

# Generating giant vortex in a Fermi superfluid via spin-orbital-angular-momentum coupling

Ke-Ji Chen,<sup>1,\*</sup> Fan Wu,<sup>1,\*</sup> Shi-Guo Peng,<sup>2</sup> Wei Yi,<sup>3,4,†</sup> and Lianyi He<sup>1,‡</sup>

<sup>1</sup>*Department of Physics and State Key Laboratory of Low-Dimensional Quantum Physics, Tsinghua University, Beijing 100084, China*

<sup>2</sup>*State Key Laboratory of Magnetic Resonance and Atomic and Molecular Physics, Wuhan Institute of Physics and Mathematics, Chinese Academy of Sciences, Wuhan, 430071, China*

<sup>3</sup>*CAS Key Laboratory of Quantum Information, University of Science and Technology of China, Hefei 230026, China*

<sup>4</sup>*CAS Center For Excellence in Quantum Information and Quantum Physics, Hefei 230026, China*

Spin-orbital-angular-momentum (SOAM) coupling has been realized in recent experiments of Bose-Einstein condensates [Chen *et al.*, Phys. Rev. Lett. **121**, 113204 (2018) and Zhang *et al.*, Phys. Rev. Lett. **122**, 110402 (2019)], where the orbital angular momentum imprinted upon bosons directly leads to quantized vortices. However, an *s*-wave Fermi pairing superfluid under the same SOAM coupling is typically vortex-less, as the two fermion species acquire opposite angular momenta in the center-of-mass motion. Here we show that, by introducing a moderate two-photon detuning in the Raman process generating the SOAM coupling, a quantized vortex, with size comparable to the beam waist of Raman lasers, can be stabilized in a Fermi superfluid. Such a giant vortex state can be viewed as the angular analogue of the Fulde-Ferrell states under a spin-orbit-coupling-induced Fermi-surface deformation, now with Cooper pairs carrying quantized angular momenta. Due to the spin-polarized nature of vortex bound states, these vortices feature a large spin polarization at the vortex core, thus providing an ideal signal for their experimental detection.

In the past decade, the experimental implementation of synthetic spin-orbit coupling (SOC) in cold atoms has stimulated extensive activities in simulating exotic quantum matter [1–9]. Under a Raman-induced SOC for instance, the internal hyperfine spins of an atom are coupled with the atomic center-of-mass momentum through a two-photon Raman process, such that the atom is subject to a non-Abelian synthetic gauge field that qualitatively modifies the single-particle dispersion, with highly non-trivial few- and many-body consequences [10–18]. Recently, an alternative type of synthetic gauge field is introduced where hyperfine spins are coupled with the atomic center-of-mass angular momentum [19–25]. Such a spin-orbital-angular-momentum (SOAM) coupling has already been experimentally demonstrated in spinor Bose-Einstein condensates (BECs), under a Raman process driven by two Laguerre-Gaussian lasers with different orbital angular momenta [26, 27]. While it has been shown that the SOAM coupling gives rise to spin-dependent vortex formation and rich quantum phases in BECs [19–28], its impact on fermions is yet to be explored. In light of the exotic pairing states in spin-orbit coupled Fermi gases [7], it would be particularly intriguing to examine the interplay between SOAM coupling and pairing in ultracold fermions.

In this Letter, we study pairing phases in a two-component Fermi gas under SOAM coupling, focusing on the vortex formation therein. Unlike the SOAM-coupled BEC, where the orbital-angular momentum imprinted upon single atoms by the Raman beams directly leads to quantized vortices in the condensate [26, 27], SOAM coupling alone does not induce vortices in a Fermi superfluid. This is understandable as fermions in a Cooper pair

acquire opposite orbital-angular momenta under SOAM coupling, which cancel each other and give rise to a superfluid state devoid of vortices. However, we show that vortices *can* be stabilized by introducing a moderate two-photon detuning in the Raman process generating the SOAM coupling. As the Raman coupling and two-photon detuning respectively serve as effective Zeeman fields in the transverse and longitudinal directions, their interplay with the SOAM coupling and pairing interactions give rise to stable vortices under experimentally achievable parameters. The underlying mechanism of the vortex formation is reminiscent of that of the SOC-enhanced Fulde-Ferrell pairing, where Cooper pairs inevitably carry finite center-of-mass momentum due to the deformation of the SOC-dressed Fermi surface under Zeeman fields [10–16]. An angular analogue of the Fulde-Ferrell pairing state, SOAM-coupling-induced vortices feature Cooper pairs with quantized angular momenta, and are easier to detect due to their topological nature.

We confirm such a vortex formation mechanism by solving the Bogoliubov-de Gennes (BdG) equation. Based on the quasi-particle spectrum, we find two vortex states: a fully gapped vortex state and a gapless one. A striking feature of these vortices is that their dynamic details, such as the order-parameter or density profiles, vary on a length scale comparable to the waist of Raman beams. This is distinct from previously studied vortices in atomic Fermi superfluids, where changes in the vortex-core structure predominantly take place within a short length scale set by the interatomic separation [29, 30]. Furthermore, we show that the vortex core exhibits a large spin imbalance, which originates from spin-polarized vortex bound states, or the so-called

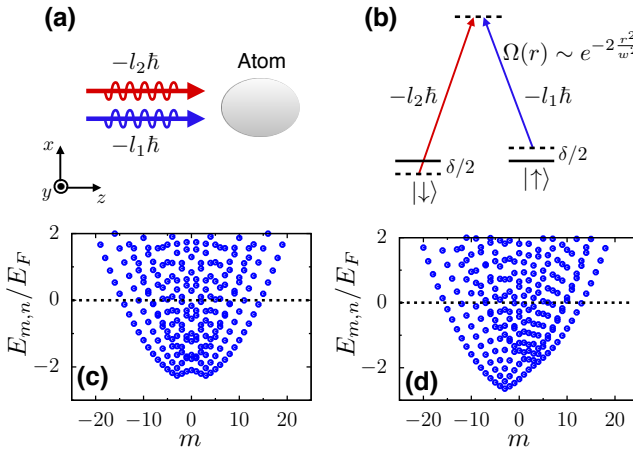


FIG. 1. (a) A pair of co-propagating Raman beams carrying different orbital angular momenta ( $-l_1\hbar$  and  $-l_2\hbar$ ) induce SOAM coupling in atoms, with a transferred angular momentum  $l\hbar = (l_1 - l_2)\hbar/2$ . (b) Schematic illustration of the level scheme. (c)(d) Single-particle energy spectra under SOAM coupling for  $\delta = 0$  (c), and  $\delta/E_F = 0.4$  (d). Black dashed lines denote potential Fermi surfaces in a many-body setting. The parameters are chosen as  $l = 3$ ,  $\Omega_0/E_F = 0.2$ ,  $k_F w = 15$  and  $k_F R = 15$ . Here the Fermi wave vector  $k_F$  is defined through the density  $n_0 = k_F^2/(2\pi)$  of a uniform Fermi gas in the area  $S = \pi R^2$ , and  $E_F = \hbar^2 k_F^2/(2M)$ , with  $M$  the atomic mass.

Caroli-de Gennes-Matricon (CdGM) states, and would serve as an ideal experimental signal for future detection. Our results offer an intriguing way of generating vortices with tunable size in a Fermi superfluid, and would stimulate further study of SOAM coupling in strongly interacting Fermi gases.

*Model:*— We consider a two-component Fermi gas confined in the two-dimensional  $x$ – $y$  plane, with different hyperfine spin states denoted by  $\uparrow$  and  $\downarrow$ , respectively. As illustrated in Fig. 1(a) and (b), the SOAM coupling is driven by a pair of co-propagating Raman beams carrying different orbital angular momenta  $-l_1\hbar$  and  $-l_2\hbar$  [31]. The two-photon Raman process is characterized by an inhomogeneous Raman coupling  $\Omega(r)$  and a phase winding  $e^{-2il\theta}$ , where  $2l \equiv l_1 - l_2$  and we adopt the polar coordinates  $\mathbf{r} = (r, \theta)$ . After a unitary transformation, the effective single-particle Hamiltonian becomes [27, 31]

$$\mathcal{H}_s = -\frac{\hbar^2}{2Mr} \frac{\partial}{\partial r} \left( r \frac{\partial}{\partial r} \right) + \frac{(L_z - l\hbar\sigma_z)^2}{2Mr^2} + \Omega(r)\sigma_x + \frac{\delta}{2}\sigma_z + V_{\text{ext}}(\mathbf{r}), \quad (1)$$

where  $M$  is the atom mass, and  $\sigma_i$  ( $i = x, y, z$ ) are the Pauli matrices. The atomic orbital angular momentum perpendicular to the  $x$ – $y$  plane,  $L_z = -i\hbar\partial/\partial\theta$ , is coupled to the atomic spin through the SOAM-coupling term  $-l\hbar L_z \sigma_z/(Mr^2)$ . The atoms are subject to an external

potential  $V_{\text{ext}}(\mathbf{r})$  in the  $x$ – $y$  plane, which we take as an isotropic hard-wall box potential with a radius  $R$ .

The Raman coupling  $\Omega(r)$  and two-photon detuning  $\delta$  provide effective transverse and longitudinal Zeeman fields, respectively, which play key roles in stabilizing vortices. While the Laguerre-Gaussian Raman beams were used in previous experiments [26, 27], their intensities are suppressed near  $r = 0$ , leading to vanishingly small SOAM-coupling effects in the vicinity which we find unfavorable for vortex formation. Instead, we consider a Gaussian-type Raman intensity, with  $\Omega(r) = \Omega_0 e^{-2r^2/w^2}$ ,  $\Omega_0$  being the intensity at the center and  $w$  the waist of lasers. Such an intensity profile can be achieved by directly imaging Raman beams with distinct orbital angular momenta onto atoms, before the beams propagate into the diffraction far field [31].

Assuming  $s$ -wave contact interactions between different spin components, the many-body Hamiltonian is given by  $H = H_0 + H_{\text{int}}$ , with  $H_0 = \int d\mathbf{r} \Psi^\dagger(\mathbf{r}) \mathcal{H}_s \Psi(\mathbf{r})$ , and  $H_{\text{int}} = -g \int d\mathbf{r} \psi_\uparrow^\dagger(\mathbf{r}) \psi_\downarrow^\dagger(\mathbf{r}) \psi_\downarrow(\mathbf{r}) \psi_\uparrow(\mathbf{r})$ . Here  $\Psi(\mathbf{r}) = [\psi_\uparrow(\mathbf{r}), \psi_\downarrow(\mathbf{r})]^T$ , with  $\psi_\sigma(\mathbf{r})$  ( $\sigma = \uparrow, \downarrow$ ) denoting the field operators for the two hyperfine spins. The bare interaction  $g$  is renormalized in two dimensions as  $g = 4\pi\hbar^2/[M \ln(1 + 2E_c/E_B)]$ , where  $E_B$  is the two-body binding energy in the absence of SOAM coupling, and  $E_c$  is a large energy cutoff to be used in the BdG calculation. Note that our results are independent of  $E_c$ .

*Single-particle spectrum:*— Before moving to the many-body BdG calculation, we first analyze the single-particle properties, i.e., the spectrum of  $\mathcal{H}_s$ , which is helpful for understanding the mechanism of vortex formation. Due to the rotational symmetry, the eigen wave function of  $\mathcal{H}_s$  can be written as  $\psi_{mn}(\mathbf{r}) = \varphi_{mn}(r)\Theta_m(\theta)$ , where the angular and radial wave functions are given by  $\Theta_m(\theta) = e^{im\theta}/\sqrt{2\pi}$  and  $\varphi_{mn}(r)$ , respectively, with  $m \in \mathbb{Z}$  and  $n \in \mathbb{Z}^+$  the corresponding quantum numbers. We numerically solve the Schrödinger equation  $\mathcal{H}_s \psi_{mn}(\mathbf{r}) = E_{m,n} \psi_{mn}(\mathbf{r})$  in the basis of the Bessel functions to determine the energy spectrum  $E_{m,n}$ . This amounts to writing  $\varphi_{mn}(r) = [f_{\uparrow mn}(r), f_{\downarrow mn}(r)]^T$ , and making the expansion  $f_{\sigma mn}(r) = \sum_{n'} c_{\sigma mn}^{(n')} R_{n',m-l\tau}(r)$ , where  $R_{n,m}(r) = \sqrt{2} J_m(\alpha_{nm} r/R) / R J_{m+1}(\alpha_{nm})$ , with  $\tau = +1$  ( $-1$ ) for  $\sigma = \uparrow$  ( $\downarrow$ ). Here  $J_m(x)$  is the Bessel function of the first kind whose zeros are given by  $\alpha_{nm}$ .

Crucially, the impact of the detuning  $\delta$  on the eigen spectrum is illustrated in Fig. 1(c) and (d). For  $\delta = 0$ , an inversion symmetry exists in the eigen spectrum, leading to a symmetric distribution of eigen energies with respect to  $m = 0$ , with  $E_{m,n} = E_{-m,n}$ . In contrast, for nonzero  $\delta$ , the inversion symmetry is broken, with  $E_{m,n} \neq E_{-m,n}$ , leading to deformed Fermi surfaces in a many-body setting.

When the attractive interaction is turned on, pairing should predominantly take place between unlike spins with the same radial quantum number  $n$  in order to max-

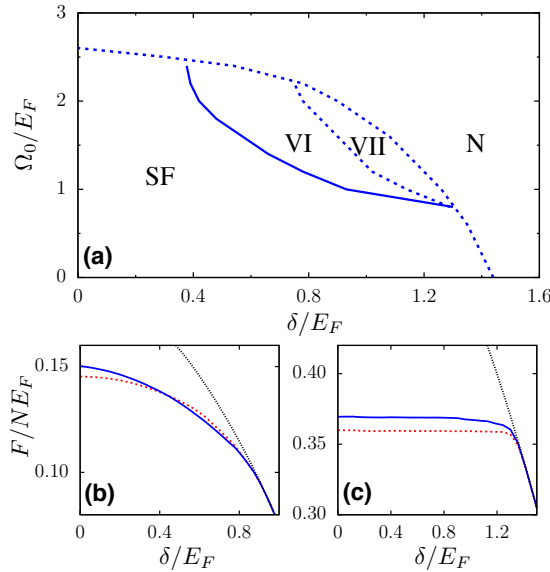


FIG. 2. (a) Phase diagram of a two-dimensional Fermi superfluid with SOAM coupling in the  $\Omega_0/E_F$ - $\delta/E_F$  plane. The angular momentum transfer is taken to be  $l\hbar = 3\hbar$  and the interaction strength is chosen as  $E_B/E_F = 0.5$ . The phase diagram includes the usual superfluid state (SF) with  $\kappa = 0$ , the normal state (N) with  $\Delta = 0$ , and two vortex states with  $\kappa = -1$ : a fully gapped vortex state (VI) and a gapless vortex state (VII). (b)(c) Free energies  $F$  of the superfluid, normal, and vortex states as functions of  $\delta$ , with  $\Omega_0/E_F = 2$  (b) and  $\Omega_0/E_F = 0.5$  (c). The parameters  $k_Fw$  and  $k_FR$  are the same as those in Fig. 1.

imize the overlap of radial wave functions. Thus, for the symmetric eigen spectrum under  $\delta = 0$ , it is more favorable for two fermions with opposite angular quantum numbers ( $m$  and  $-m$ ) to form a Cooper pair, carrying a vanishing total angular momentum. In contrast, under a finite  $\delta$  with asymmetric eigen spectrum, the two fermions in a Cooper pair may possess different values of  $|m|$ , resulting in a pairing state with a nonzero, quantized angular momentum, which is nothing but a Fermi superfluid with vortices. Such a mechanism for the vortex formation is analogous to that of the SOC-induced Fulde-Ferrell pairing in spin-orbit coupled Fermi gases, where the interplay between SOC and Zeeman fields leads to the deformation of Fermi surfaces with broken inversion symmetry in the momentum space [12–16]. However, a key difference here is the quantization of the angular momentum, which gives rise to topological defects in the resulting Fermi superfluid.

*BdG formalism:*— We confirm the analysis above by solving the many-body problem under the BdG formalism. The BdG equation is given by  $\mathcal{H}_{\text{BdG}}\Phi_{mn}(\mathbf{r}) =$

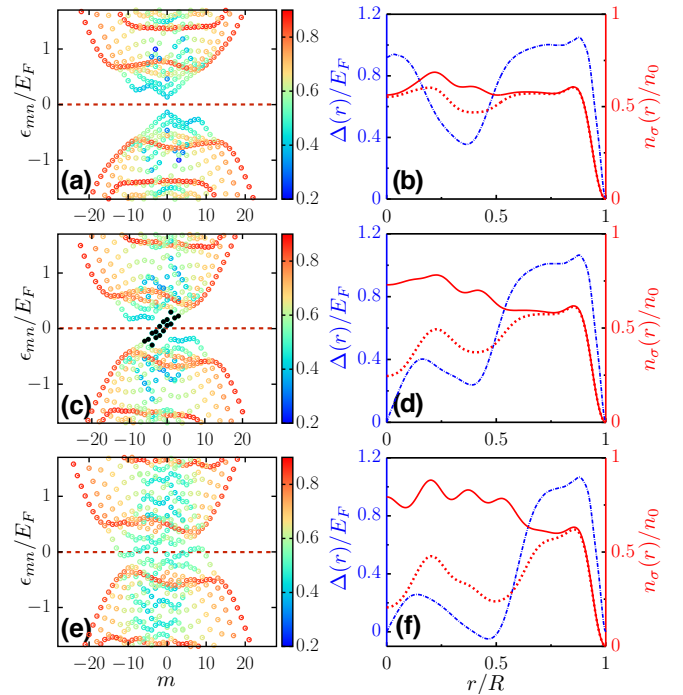


FIG. 3. Energy spectra and vortex-core structures for the SF state with  $\delta/E_F = 0.48$  [(a)(b)], the VI state with  $\delta/E_F = 0.84$  [(c)(d)], and the VII state with  $\delta/E_F = 1.035$  [(e)(f)]. In the energy spectra (a)(c)(e), different eigenstates are color-coded according to the ratio  $\sqrt{\langle r^2 \rangle}/R$ , with the root-mean-square of the radius  $\langle r^2 \rangle = \sum_{\sigma} \int dr r^2 (|u_{\sigma mn}|^2 + |v_{\sigma mn}|^2)$ . The CdGM states are indicated by black dots in (c). In (b)(d)(f), the blue dash-dotted correspond to the order parameter profile, and red solid (dashed) lines are the radial density profiles of the spin-down (up) atoms, respectively. The radial density is calculated through  $n_{\sigma}(r) = \frac{1}{2\pi} \int d\theta n_{\sigma}(\mathbf{r})$ . Here we take  $\Omega_0/E_F = 1.2$  and other parameters are the same as those in Fig. 2.

$\epsilon_{mn}\Phi_{mn}(\mathbf{r})$ , with

$$\mathcal{H}_{\text{BdG}} = \begin{bmatrix} K_{\uparrow}(\mathbf{r}) & \Omega(r) & 0 & \Delta(\mathbf{r}) \\ \Omega(r) & K_{\downarrow}(\mathbf{r}) & -\Delta(\mathbf{r}) & 0 \\ 0 & -\Delta^*(\mathbf{r}) & -K_{\uparrow}^*(\mathbf{r}) & -\Omega(r) \\ \Delta^*(\mathbf{r}) & 0 & -\Omega(r) & -K_{\downarrow}^*(\mathbf{r}) \end{bmatrix}. \quad (2)$$

Here  $\Phi_{mn}(\mathbf{r}) = [u_{\uparrow mn}, u_{\downarrow mn}, v_{\uparrow mn}, v_{\downarrow mn}]^T$ , with  $u_{\sigma mn}$  and  $v_{\sigma mn}$  being the Bogoliubov coefficients, and  $K_{\sigma}(\mathbf{r}) = -\frac{\hbar^2}{2M} \left[ \frac{1}{r} \frac{\partial}{\partial r} (r \frac{\partial}{\partial r}) + \frac{1}{r^2} (\frac{\partial}{\partial \theta} - i\tau l)^2 \right] + \tau \frac{\delta}{2} - \mu$ . The chemical potential  $\mu$  is introduced to fix the total particle number  $N$ . The superfluid order parameter  $\Delta(\mathbf{r}) = -g\langle\psi_{\downarrow}(\mathbf{r})\psi_{\uparrow}(\mathbf{r})\rangle$  should be determined through the self-consistent equation

$$\Delta(\mathbf{r}) = \frac{g}{2} \sum_{mn} \left[ u_{\uparrow mn} v_{\downarrow mn}^* \vartheta(\epsilon_{mn}) + u_{\downarrow mn} v_{\uparrow mn}^* \vartheta(-\epsilon_{mn}) \right], \quad (3)$$

where  $\vartheta(x)$  is the Heaviside step function.

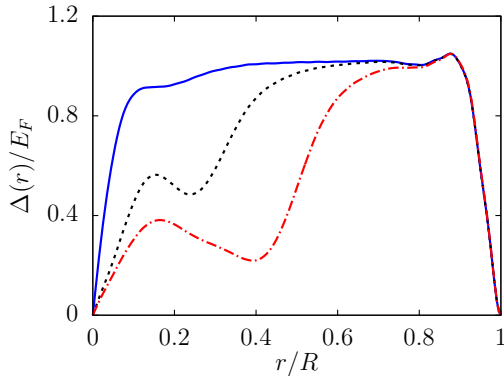


FIG. 4. Order parameter profiles for  $k_F w = 5$  (blue solid),  $k_F w = 10$  (black dashed), and  $k_F w = 15$  (red dash-dotted). We fix  $\delta/E_F = 0.84$  and  $k_F R = 15$ , with other parameters the same as those in Fig. 3.

We expect that a vortex state would be the ground state for appropriate values of  $\Omega_0$  and  $\delta$ , and thus assume that the order parameter takes the form  $\Delta(\mathbf{r}) = \Delta(r)e^{i\kappa\theta}$ , where the vorticity  $\kappa \in \mathbb{Z}$  characterizes the quantized angular momentum of the vortex. Due to the rotational symmetry, it is convenient to write  $u_{\sigma mn} = \sum_{n'} c_{\sigma mn}^{(n')} R_{n', m-\tau l}(r) \Theta_m(\theta)$ , and  $v_{\sigma mn} = \sum_{n'} d_{\sigma mn}^{(n')} R_{n', m+\tau l-\kappa}(r) \Theta_{m-\kappa}(\theta)$ . The BdG equation then becomes a matrix equation for the expansion coefficients  $c_{\sigma mn}^{(n')}$  and  $d_{\sigma mn}^{(n')}$  [31].

For different values of  $\kappa \in \mathbb{Z}$ , we solve the BdG equation and the self-consistent equation (3) under the particle number constraint  $N = \sum_{\sigma} \int d\mathbf{r} n_{\sigma}(\mathbf{r})$ , with density profiles  $n_{\sigma}(\mathbf{r}) = \frac{1}{2} \sum_{mn} [ |u_{\sigma mn}|^2 \vartheta(-\epsilon_{mn}) + |v_{\sigma mn}|^2 \vartheta(\epsilon_{mn}) ]$ . We then compare the free energies of the vortex state ( $\kappa \neq 0$ ), the usual superfluid state ( $\kappa = 0$ ), and the normal state ( $\Delta = 0$ ) to determine the phase diagram.

*Phase diagram and vortex structure:*— The phase diagram in the  $\Omega_0$ – $\delta$  plane is shown in Fig. 2(a) for the angular momentum transfer  $l\hbar = 3\hbar$  and interaction strength  $E_B/E_F = 0.5$ . For  $\delta > 0$  ( $\delta < 0$ ), vortex states with  $\kappa = -1$  ( $\kappa = 1$ ) are favored, with the phase diagram unchanged by the sign of  $\delta$ .

At small  $\Omega_0$  and  $\delta$ , the ground state is a usual superfluid (SF) with a vanishing vorticity  $\kappa = 0$ . Under sufficiently large  $\Omega_0$  and/or  $\delta$ , which play the role of effective Zeeman fields, the free-energy difference between the SF and normal (N) states becomes vanishingly small. Since beyond-mean-field fluctuations tend to stabilize the normal state, for all practical purposes, we consider the system to be in a normal state when the free-energy difference is smaller than  $10^{-3}E_F$ . More importantly, between the superfluid and normal states, two vortex states exist in a region with moderate  $\Omega_0$  and  $\delta$ . For example, with a fixed  $\Omega_0/E_F = 1.5$  [see Fig. 2(a)], the ground state

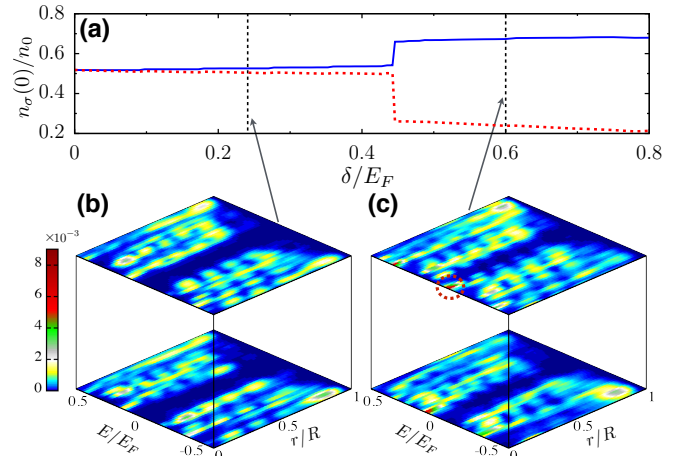


FIG. 5. (a) Densities of the two spin components at the trap center,  $n_{\sigma}(r = 0)$ , as a function of the detuning  $\delta$ . The blue solid (red dashed) curve denotes the spin-down (spin-up) component. (b) (c) Local densities of state  $D_{\sigma}(r, E)$  for  $\delta/E_F = 0.24$  (b) and  $\delta/E_F = 0.6$  (c). The upper (lower) layer shows the local density of state of the spin-down (spin-up) component. The red circle in (c) indicates the occupied CdGM state responsible for the spin imbalance at  $r = 0$ . Here we take  $\Omega_0/E_F = 2$  and other parameters are the same as those in Fig. 2.

is in the SF state under small detunings  $\delta$ , and becomes a fully-gapped vortex state (VI) beyond a critical value of  $\delta$ . Further increase of  $\delta$  leads to a gapless vortex state (VII), where the bulk excitation gap is closed.

In Fig. 2(b) and (c), we compare free energies for different states, as the phase diagram is traversed. In particular, for the case with  $\Omega_0 = 0.5E_F$ , the ground state remains vortex-less for finite  $\delta$ , despite the deformation of the Fermi surface under SOAM coupling and effective Zeeman fields. This is due to the quantized nature of the angular momentum, and is in sharp contrast to the SOC-induced Fulde-Ferrell state which always acquires a finite, continuously varying center-of-mass momentum in the presence of SOC and Zeeman fields [10–16].

In Fig. 3, we show the energy spectrum  $\epsilon_{mn}$ , the order parameter  $\Delta(r)$ , and the density profiles in the SF state [Fig. 3(a)(b)], the VI state [Fig. 3(c)(d)], and the VII state [Fig. 3(e)(f)]. In the ground state, all eigen states with  $\epsilon_{mn} < 0$  are occupied. Here two important observations are in order.

First, both the order parameter and density profiles vary over a length scale set by the laser waist  $w$ , leading to a giant vortex core with tunable size. This is clearly visible in Fig. 4, where the vortex-core size, characterized by variations of the order parameter, is comparable to  $w$ , the latter being much larger than  $k_F^{-1}$  in experiments.

Second, the order parameter  $\Delta(r)$  of either vortex states vanishes at  $r = 0$ , accompanied by a large spin imbalance near the vortex core. This is in contrast to the

SF state, where the spin population is roughly balanced at  $r = 0$  [Fig. 3(b)]. In Fig. 5(a), we show the densities of the two spin components at  $r = 0$  as a function of the detuning  $\delta$ . The spin imbalance remains small in the SF state at small  $\delta$ , but abruptly jumps to a large value once the system is in the vortex state, suggesting a discontinuous phase transition. To better characterize the large spin polarization at the vortex core, we calculate the local density of state  $D_\sigma(r, E) = \frac{1}{2\pi} \int d\theta D_\sigma(\mathbf{r}, E)$ , which offers both spatial and spectral resolution of all eigen states. Here  $D_\sigma(\mathbf{r}, E) = \frac{1}{2} \sum_{mn} [|u_{\sigma mn}|^2 \delta(E - \epsilon_{mn}) + |v_{\sigma mn}|^2 \delta(E + \epsilon_{mn})]$ . Our results for the SF and VI states are shown in Fig. 5(b) and Fig. 5(c), respectively. As indicated by the red circle in Fig. 5(c), occupied CdGM states with large spin polarization exist in the excitation gap, which are localized near  $r = 0$  with depleted pairing order parameter, effectively serving as a dump for the spin polarization under Zeeman fields. These CdGM states are directly responsible for the observed large spin polarization at the vortex core in Figs. 3(d). In the VII state, despite the closing of the bulk excitation gap, local spin polarization near the core persists, due to polarized local states that are smoothly connected to the CdGM states in the gapped phase [31].

*Discussion:*— Experimentally, the SOAM-coupling-induced vortices can be detected through the apparent spin polarization at vortex cores, which is further facilitated by their large and tunable size. For instance, with  $w \sim 7.5\mu\text{m}$  and  $l = 3$ , and under typical parameters of a quasi-two-dimensional Fermi gas of  ${}^6\text{Li}$  atoms with  $E_F \sim 2\pi\hbar \times 3.4\text{kHz}$  [35], the parameter window for a stable vortex state is  $\Omega_0 \sim 2\pi\hbar \times (3.4, 8.5)\text{kHz}$  and  $\delta \sim 2\pi\hbar \times (1.4, 4.1)\text{kHz}$ , which are readily accessible in current experiments. While we focus on the case with  $l\hbar = 3\hbar$ , an interesting question is whether quantized vortices with  $|\kappa| > 1$  can be stabilized given a larger angular-momentum transfer. Furthermore, given the rich phases of spin-orbit coupled Fermi gases, it would be fascinating to explore other exotic superfluid states induced by the SOAM coupling.

We acknowledge fruitful discussions with Jian-Song Pan, Jing Zhou and Dongyang Yu. This work was supported by the Natural Science Foundation of China (Grant Nos. 11775123, 11974331, 11974384) and the National Key R&D Program (Grant Nos. 2018YFA0306503, 2016YFA0301700, 2017YFA0304100, 2016YFA0301503).

- [3] L. W. Cheuk, A. T. Sommer, Z. Hadzibabic, T. Yefsah, W. S. Bakr, and M. W. Zwierlein, *Phys. Rev. Lett.* **109**, 095302 (2012).
- [4] V. Galitski and I. B. Spielman, *Nature (London)* **494**, 49 (2013).
- [5] N. Goldman, G. Juzeliūnas, and P. Öhberg, I. B. Spielman, *Rep. Prog. Phys.* **77**, 126401 (2014).
- [6] H. Zhai, *Rep. Prog. Phys.* **78**, 026001 (2015).
- [7] W. Yi, W. Zhang, and X. Cui, *Sci. China: Phys. Mech. Astron.* **58**, 014201 (2015).
- [8] J. Zhang, H. Hu, X. J. Liu, and H. Pu, *Ann. Rev. Cold At. Mol.* **2**, 81 (2015).
- [9] L. Zhang and X. J. Liu, arXiv:1806.05628.
- [10] L. Dong, L. Jiang, H. Hu, and H. Pu, *Phys. Rev. A* **87**, 043616 (2013).
- [11] V. B. Shenoy, *Phys. Rev. A* **88**, 033609 (2013).
- [12] F. Wu, G.-C. Guo, W. Zhang, and W. Yi, *Phys. Rev. Lett.* **110**, 110401 (2013).
- [13] C. Qu, Z. Zheng, M. Gong, Y. Xu, L. Mao, X. Zou, G. Guo, and C. Zhang, *Nat. Commun.* **4**, 2710 (2013).
- [14] W. Zhang and W. Yi, *Nat. Commun.* **4**, 2711 (2013).
- [15] C. Chen, *Phys. Rev. Lett.* **111**, 235302 (2013).
- [16] X.-J. Liu and H. Hu, *Phys. Rev. A* **88**, 023622 (2013).
- [17] Z.-Y. Shi, X. Cui, and H. Zhai, *Phys. Rev. Lett.* **112**, 013201 (2014).
- [18] X. Cui and W. Yi, *Phys. Rev. X* **4**, 031026 (2014).
- [19] Y.-X. Hu, C. Miniatura, and B. Grémaud, *Phys. Rev. A* **92**, 033615 (2015).
- [20] M. DeMarco and H. Pu, *Phys. Rev. A* **91**, 033630 (2015).
- [21] K. Sun, C. Qu, and C. Zhang, *Phys. Rev. A* **91**, 063627 (2015).
- [22] C. Qu, K. Sun, and C. Zhang, *Phys. Rev. A* **91**, 053630 (2015).
- [23] L. Chen, H. Pu, and Y. Zhang, *Phys. Rev. A* **93**, 013629 (2016).
- [24] X.-L. Chen, S.-G. Peng, P. Zou, X.-J. Liu, and H. Hu, arXiv:1901.02595 (2019).
- [25] K.-J. Chen, F. Wu, J. Hu, and L. He, arXiv: 1911.00255 (2019).
- [26] H.-R. Chen, K.-Y. Lin, P.-K. Chen, N.-C. Chiu, J.-B. Wang, C.-A. Chen, P.-P. Huang, S.-K. Yip, Y. Kawaguchi, and Y.-J. Lin, *Phys. Rev. Lett.* **121**, 113204 (2018).
- [27] D. Zhang, T. Gao, P. Zou, L. Kong, R. Li, X. Shen, X.-L. Chen, S.-G. Peng, M. Zhan, H. Pu, and K. Jiang, *Phys. Rev. Lett.* **122**, 110402 (2019).
- [28] L. Chen, Y. Zhang, and H. Pu, arXiv: 2005.08498 (2020).
- [29] R. Sensarma, M. Randeria, and T.-L. Ho, *Phys. Rev. Lett.* **96**, 090403 (2006).
- [30] C.-C. Chien, Y. He, Q. Chen, and K. Levin, *Phys. Rev. A* **73**, 041603(R) (2006).
- [31] See Supplemental Material for details.
- [32] Y. S. Rumala and A. E. Leanhardt, *J. Opt. Soc. Am. B* **34**, 909 (2017).
- [33] E. Karimi, G. Zito, B. Piccirillo, L. Marrucci, and E. Santamato, *Opt. Lett.* **32**, 3053 (2007).
- [34] C. Caroli, P. G. de Gennes, and J. Matricon, *Phys. Lett.* **9**, 307 (1964).
- [35] K. Hueck, N. Luick, L. Sobirey, J. Siegl, T. Lompe, and H. Moritz, *Phys. Rev. Lett.* **120**, 060402 (2018).

\* These authors contributed equally to this work.

<sup>†</sup> [wyiz@ustc.edu.cn](mailto:wyiz@ustc.edu.cn)

<sup>‡</sup> [lianyi@mail.tsinghua.edu.cn](mailto:lianyi@mail.tsinghua.edu.cn)

- [1] Y.-J. Lin, K. Jiménez-García, and I. B. Spielman, *Nature (London)* **471**, 83 (2011).
- [2] P. Wang, Z.-Q. Yu, Z. Fu, J. Miao, L. Huang, S. Chai, H. Zhai, and J. Zhang, *Phys. Rev. Lett.* **109**, 095301 (2012).

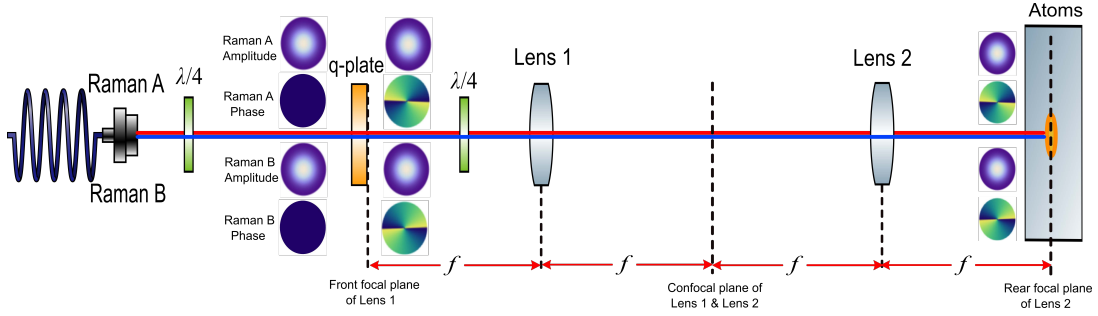


FIG. S1. A simplified illustration of the proposed optical setup. A pair of Gaussian Raman beams, Raman *A* and Raman *B*, emerge from the same optical fiber with orthogonal linear polarizations (the red and blue straight lines with slight lateral shift to guide the eye). They are transformed into circularly polarized ones by a quarter-wave plate to acquire a winding phase  $e^{\pm il\theta}$  from the *q*-plate (depending on their polarizations). The Raman beams are then transformed back to linear polarizations again by a quarter-wave plate. The Gaussian-type profiles right after the *q*-plate with winding phases  $e^{\pm il\theta}$  are imaged by a 4*f*-lens system onto the atoms placed on the rear plane.

### Supplemental Material for “Generating giant vortex in a Fermi superfluid via spin-orbital-angular-momentum coupling”

In this Supplemental Material, we provide details on the experimental implementation, derivation of the effective single-particle Hamiltonian, the matrix form of the BdG equation, as well as the spectrum of the gapless vortex state.

#### Experimental implementation

In this section, we provide details on an experimental proposal for implementing a Gaussian-type Raman coupling. As illustrated in Fig. S1, phase patterns  $e^{+il\theta}$  and  $e^{-il\theta}$  are imprinted by a *q*-plate respectively on the input pair of Gaussian beams with different circular polarizations. Subsequently, a 4*f*-lens system is employed to image the Gaussian intensity profile immediately after the *q*-plate onto the atoms [32]. Unlike the situations in previous works [26, 27], here we use the beam profile right after the *q*-plate and do not allow it to further propagate into the diffraction far field, thus avoiding the Laguerre function and the factor  $|r|^l$  to appear in the intensity profile.

#### Effective single-particle Hamiltonian

In this section, we briefly outline the derivation of the effective single-particle Hamiltonian Eq. (1) in the main text. We start from considering a pair of co-propagating Raman beams carrying different angular momenta, which couple two hyperfine states ( $\uparrow$  and  $\downarrow$ ) of an atom. After the adiabatic elimination of the excited states, the effective single-particle Hamiltonian in the hyperfine-spin basis reads

$$\mathcal{H}_0 = \begin{bmatrix} -\frac{\hbar^2 \nabla^2}{2M} + V_{\text{ext}}(\mathbf{r}) + \frac{\delta}{2} & \Omega(r) e^{-i(l_1 - l_2)\theta} \\ \Omega(r) e^{i(l_1 - l_2)\theta} & -\frac{\hbar^2 \nabla^2}{2M} + V_{\text{ext}}(\mathbf{r}) - \frac{\delta}{2} \end{bmatrix}, \quad (\text{S1})$$

where  $\nabla^2 = \frac{1}{r} \frac{\partial}{\partial r} (r \frac{\partial}{\partial r}) + \frac{1}{r^2} \frac{\partial^2}{\partial \theta^2}$ , and the phase windings  $e^{-il_i\theta}$  ( $i = 1, 2$ ) reflect the orbital angular momenta  $-l_i \hbar$  carried by the two Raman beams. The two-photon Raman coupling and detuning are denoted by  $\Omega(r)$  and  $\delta$ , respectively. The atoms are confined in an external potential denoted by  $V_{\text{ext}}(\mathbf{r})$ .

The phase terms in the off-diagonal components can be eliminated via a unitary transformation  $\mathcal{H}_s = U^\dagger \mathcal{H}_0 U$ , where  $U = \text{diag}(e^{-il\theta}, e^{il\theta})$ , with  $l = (l_1 - l_2)/2$ . We thus arrive at the effective single-particle Hamiltonian  $\mathcal{H}_s$ , given by Eq. (1) in the main text.

#### BdG equation in the Bessel-function basis

Based on the expansion of  $u_{\sigma mn}$  and  $v_{\sigma mn}$  in terms of the Bessel-function basis, as shown in the main text, the BdG equation (2) becomes decoupled in each  $m$  sector. For a given  $m$ , the BdG equation can be expressed as a matrix

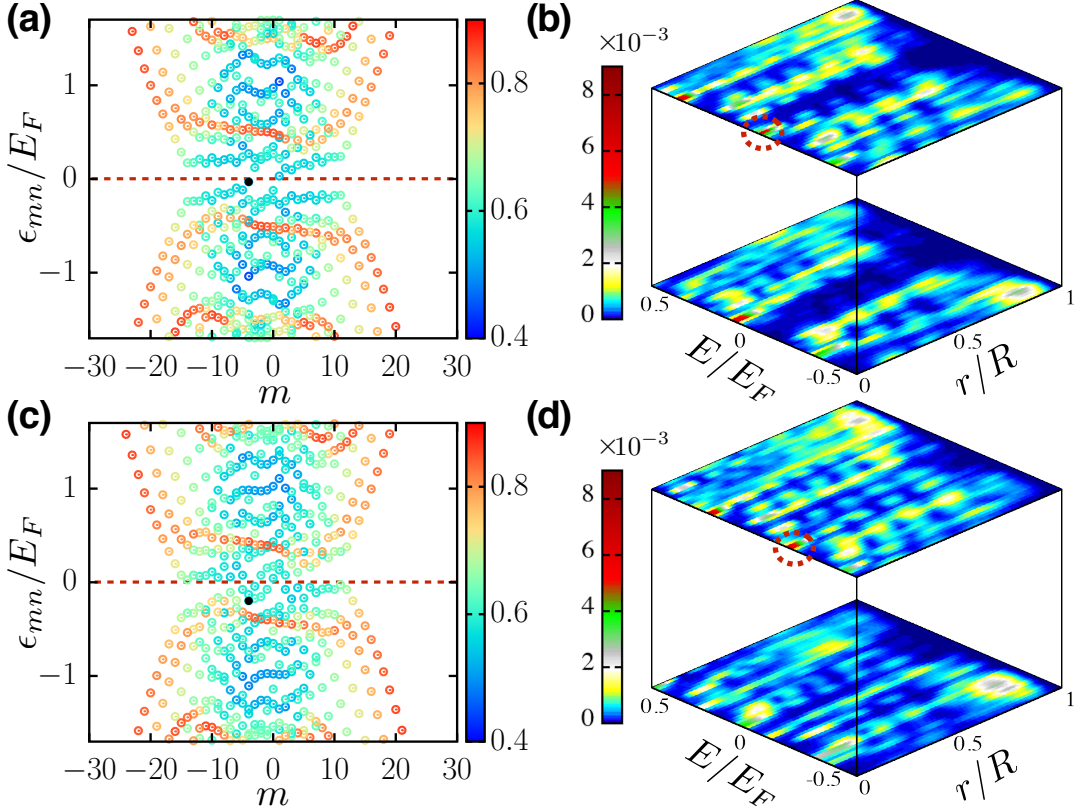


FIG. S2. Energy spectrum and local densities of state  $D_\sigma(r, E)$  for (a)(b) gapped vortex state with  $\delta/E_F = 0.48$ , and (c)(d) gapless vortex state with  $\delta/E_F = 0.84$ . For the fully-gapped vortex state in (a), most of the spin polarizations at the vortex core is carried by the occupied CdGM state marked in black, which is also circled out in  $D_\sigma(r, E)$  (b). For the gapless vortex in (c), spin polarization again concentrates near  $r = 0$  and is carried by a state (in black) that can be smoothly connected to the CdGM state in (a). In (b)(d), the upper (lower) layer shows the local densities of state of the spin-down (spin-up) component. Here we take  $\Omega_0/E_F = 2$ , while other parameters are the same as those in Fig. 2. See also Fig. 3 for the convention of color coding.

equation for the expansion coefficients  $c_{\sigma mn}^{(n')}$  and  $d_{\sigma mn}^{(n')}$ ,

$$\sum_{n''} \begin{bmatrix} K_{\uparrow, m-l}^{n' n''} & \Omega_{n', m-l}^{n'', m+l} & 0 & \Delta_{n', m-l-\kappa}^{n'', m-l-\kappa} \\ \Omega_{n', m+l}^{n'' n''} & K_{\downarrow, m+l}^{n', m+l} & -\Delta_{n', m+l}^{n'', m+l-\kappa} & 0 \\ 0 & -\Delta_{n', m+l-\kappa}^{n'', m+l} & -K_{\uparrow, m+l-\kappa}^{n', m+l-\kappa} & -\Omega_{n', m+l-\kappa}^{n'', m+l-\kappa} \\ \Delta_{n', m-l-\kappa}^{n'', m-l} & 0 & -\Omega_{n', m-l+\kappa}^{n'', m+l-\kappa} & -K_{\downarrow, m-l-\kappa}^{n', n''} \end{bmatrix} \begin{bmatrix} c_{\uparrow mn}^{(n'')} \\ c_{\downarrow mn}^{(n'')} \\ d_{\uparrow mn}^{(n'')} \\ d_{\downarrow mn}^{(n'')} \end{bmatrix} = \epsilon_{mn} \begin{bmatrix} c_{\uparrow mn}^{(n')} \\ c_{\downarrow mn}^{(n')} \\ d_{\uparrow mn}^{(n')} \\ d_{\downarrow mn}^{(n')} \end{bmatrix}. \quad (\text{S2})$$

The elements are given by

$$K_{\sigma, p}^{n' n''} = \left( \frac{\hbar^2 \alpha_{n', p}^2}{2mR^2} + \tau \frac{\delta}{2} - \mu \right) \delta_{n' n''}, \quad (\text{S3})$$

$$\Omega_{n', p}^{n'', q} = \int r dr R_{n', p}(r) \Omega(r) R_{n'', q}(r), \quad (\text{S4})$$

$$\Delta_{n', p}^{n'', q} = \int r dr R_{n', p}(r) \Delta(r) R_{n'', q}(r). \quad (\text{S5})$$

For a given profile of  $\Delta(r)$ , we diagonalize the matrix in Eq. (S2) to determine the quasiparticle spectrum  $\epsilon_{mn}$  and the coefficients  $c_{\sigma mn}^{(n')}$  and  $d_{\sigma mn}^{(n')}$ . The profile  $\Delta(r)$  and the chemical potential  $\mu$  are then determined through the self-consistent equation and the number equation given in the main text. The free energy of the pairing state can be

evaluated as

$$F = \frac{1}{2} \sum_{mn} \epsilon_{mn} \left[ \vartheta(-\epsilon_{mn}) - \sum_{\sigma} \int d\mathbf{r} |v_{\sigma mn}(\mathbf{r})|^2 \right] + \int d\mathbf{r} \frac{|\Delta(\mathbf{r})|^2}{g} + \mu N. \quad (\text{S6})$$

#### Energy spectrum and local density of states for gapless vortices

For a fully-gapped vortex, the majority of the spin polarization at  $r = 0$  is carried by a single occupied ( $\epsilon_{mn} < 0$ ) CdGM state, as illustrated in Fig. S2(a)(b). When increasing  $\delta$ , the vortex state can become gapless. Despite the closing of the bulk gap, the heavily-polarized CdGM state is smoothly connected to an extended state in the gapless spectrum, which is also heavily polarized at  $r = 0$  [see Fig. S2(c)(d)]. As such, both gapped and gapless vortices are amenable to our proposed detection scheme.